Photoelectron holography in strong-field tunneling ionization by a spatially inhomogeneous field

Yongkun Chen [,1] Yueming Zhou [,1,*] Jia Tan,[1,2] Min Li [,1] Wei Cao,[1] and Peixiang Lu[1,3,4,†]

[1]*School of Physics and Wuhan National Laboratory for Optoelectronics,*
Huazhong University of Science and Technology, Wuhan 430074, China
[2]*Jiangsu Key Laboratory of Micro and Nano Heat Fluid Flow Technology and Energy Application, School of Physical Science*
and Technology, Suzhou University of Science and Technology, Suzhou, 215009, China
[3]*Hubei Key Laboratory of Optical Information and Pattern Recognition, Wuhan Institute of Technology, Wuhan 430205, China*
[4]*CAS Center for Excellence in Ultra-intense Laser Science, Shanghai 201800, China*

Photoelectron holography in strong-field tunneling ionization is an efficient way to probe the structures and the ultrafast dynamics information of atoms and molecules. Manipulating the process of photoelectron holography is important for its application. Here, we study theoretically strong-field photoelectron holography in the spatially inhomogeneous field by solving the time-dependent Schrödinger equation. Our results show that the returning energy of the rescattering electron is greatly enhanced in the spatially inhomogeneous field, and the holographic interference pattern can be separated from other types of interference in the photoelectron momentum distribution. Moreover, our results show that the time window of tunneling ionization wherein the electron could be driven back to induce holography is broadened in the inhomogeneous field. These properties are beneficial for the application of photoelectron holography in probing the atomic and molecular structures and dynamics. The origin for these properties is analyzed with the classical trajectory model.

I. INTRODUCTION

Strong-field tunneling ionization is a fundamental process in laser-matter interactions. The tunneling process gives rise to many important phenomena, such as high-order harmonic generation (HHG) [1], above-threshold ionization (ATI) [2], and nonsequential double ionization (NSDI) [3,4]. With the semiclassical three-step model, the process can be described well [5,6]. When a laser field interacts with an atom or molecule, the bound electron is tunneling-ionized through the potential barrier. The ionized electron is further accelerated by oscillation laser field. Depending on the tunneling ionization time, the electron can return to the vicinity of the parent ion and interact with it to produce ATI, HHG, or NSDI. During the past decades, the rescattering process has attracted increasing interest, and it has been widely applied in attosecond pulse generation [7], laser-induced electron diffraction [8], molecular orbital tomography [9], etc.

Due to the coherent nature of the electron wave packets (EWPs), the tunneling ionized electron that interacts with the parent ion before reaching the detector (rescattering electron) can interfere with that without interaction with the parent ion (direct electron), results in strong-field photoelectron holography (SFPH) [10]. The holographic structure was first observed in experiments for xenon [10] and then observed in other atoms and molecules [11–15]. It is believed that SFPH is an efficient way to probe the atomic and molecular structures and the ultrafast electron dynamics [16–30]. Recently, we

have shown that with the concept of SFPH, the phase of the elastic-scattering amplitude could be retrieved [21]. More interestingly, the attosecond charge migration in molecules could also be probed with unprecedented temporal and spatial resolutions [22]. The tunneling ionization process itself could also be probed with SFPH. For example, it has been shown that the hologram in the photoelectron momentum distribution (PEMD) encodes the phase structure of the tunneled electron wave packet [15,18]. This phase structure is directly related to the launching position of the tunneling electron wave packet [27]. Therefore, the initial transverse displacement of the EWP from molecular strong-field tunneling ionization has been successfully retrieved [27]. Moreover, with the concept of SFPH, the correspondence between the tunneling ionization time and final electron momentum [17], and the initial longitudinal momentum of the tunneled electron [19] have been deeply surveyed.

Previous studies of SFPH mostly focused on the spatially homogeneous field. In recent years, the strong-field ionization phenomena in the spatially inhomogeneous field have attracted much attention [31–59]. When a laser pulse illuminated on a metal nanostructure, the near-field is greatly enhanced and becomes spatially inhomogeneous in the vicinity of the nanostructure [41]. The spatial inhomogeneity of the near-field can alter the electron dynamics, and its effect can be characterized by the parameter $\delta = l_F/l_q$, where l_F is the decay length of the enhanced field and $l_q = eE/m\omega^2$ is the electron quiver amplitude [31]. For $\delta \gg 1$, the electron approximately quivers in a homogeneous field. For $\delta \ll 1$, the electron rapidly leaves the vicinity of the nanostructure. Previous works mainly focused on the regime of $\delta \approx 1$, where the electrons can be effected by the spatial inhomogeneity to

the greatest extent. In the inhomogeneous field, the trajectories of the electrons after ionization are very different from that in homogeneous field. With the development of related research, many interesting phenomena and applications have been found. For example, the electron ionized from the inhomogeneous field can gain a higher energy, even to the keV regime [34,57]. This high energy leads the extension of the harmonic cutoff [41–44]. In addition, the potential symmetry is broken by the spatial inhomogeneity, and thus the odd and even harmonics appear simultaneously [41,42]. Moreover, the electron trajectory is modified by the inhomogeneous field, which provides a condition for the generation of pulses with picometer spatial and attosecond temporal [45–47]. Furthermore, through numerically solving the three-dimensional time-dependent Schrödinger equation (3 D-TDSE), it is found that the electron momentum distribution is sensitive to the carrier envelope phase (CEP) of the laser field [38], and the higher-energy structure in strong-field ionization is related to the decay length l_F [39]. The latter can provide tool for near-field characterization [39]. Very recently, it has demonstrated that changing the direction of the enhanced field can control the electron trajectories and modify the ellipticity of the emitted attosecond pulses [40]. The spatially inhomogeneous field has also been applied to molecules. For H_2^+ in the inhomogeneous field, a photodissociation path, two-step transition mediated by vibrationally excited states, is opened [55], and the electron localization can be controlled [56].

In this study, we theoretically study the SFPH in the spatially inhomogeneous field. The PEMDs are obtained by numerically solving the two-dimensional TDSE. We demonstrate that the electrons ionized in different cycles can be separated in the momentum space, and the holographic interference patterns can be separated from other types of interference. With the classical trajectory model, we show that the time window of tunneling ionization, wherein the electron rescatters with the parent ion to induce holography, can be broaden in the inhomogeneous field. In addition, it also shows that the significant increasing of the electron energy and the change of the travel time originate from the spatial inhomogeneity. By changing the CEP and the strength of spatial inhomogeneity, the effect of the spatial inhomogeneity on the trajectories can be controlled. These properties benefit the application of photoelectron holography in probing the atomic and molecular structures and dynamics.

II. NUMERICAL METHODS

To investigate the tunneling ionization driven by the spatially inhomogeneous field, we numerically solve the two-dimensional TDSE (2D-TDSE) with the single-active-electron (SAE) approximation. The TDSE reads [atomic units (a.u.) are used throughout unless stated otherwise]

$$i\frac{\partial \Psi(\vec{r}, t)}{\partial t} = H(\vec{r}, t)\Psi(\vec{r}, t), \tag{1}$$

where $H(\vec{r}, t)$ is the Hamiltonian. In the length gauge, it reads

$$H(\vec{r}, t) = \frac{1}{2}\Delta^2 + V_{\text{atom}}(\vec{r}) + V_{\text{laser}}(\vec{r}, t), \tag{2}$$

where $V_{\text{atom}}(\vec{r})$ is the atomic potential and $V_{\text{laser}}(\vec{r})$ represents the potential due to the laser field. We choose the effective

soft-core potential to describe the atomic potential:

$$V_{\text{atom}}(\vec{r}) = -\frac{1}{\sqrt{x^2 + y^2 + a}}, \tag{3}$$

where a is the soft parameter, which is set to be 0.65 to match the ground-state energy of hydrogen ($I_p = 0.5$ a.u.). Nanostructure with different shapes can generate different spatially inhomogeneous field, which has a different influence on the trajectories of electrons [47]. We consider the spatially inhomogeneous field generated by a nanotip, which decays exponentially. In previous work, this field is approximated as linearly decreasing, and this approximation is widely used in the study of the electron dynamics in the inhomogeneous fields [34–42]. With this approximation, the laser field can be written as

$$\vec{E}(\vec{r}, t) = E_0(1 + 2\varepsilon x)f(t)\sin(\omega t + \phi)\hat{x}. \tag{4}$$

Here, ϕ is the CEP, $\omega = 0.0285$ a.u. is the central frequency of the 1600-nm laser field, and $f(t)$ is the pulse envelope which has a $\sin^2(\pi t/T_p)$ form with a duration of $T_p = 4T$, where T is optical cycle period of the laser field. The intensity I of the 1600-nm laser field is fixed at 1×10^{14} W/cm^2. ε is another parameter characterizing the "strength" of the spatial inhomogeneity, and the relation between ε and decay length is $l_F = 1/2\varepsilon$. We take two cases, $\varepsilon = 0.003$ ($l_F = 8.3$ nm), corresponding to the inhomogeneous field where $\delta = 2.53$, and $\varepsilon = 0$, which means the spatially homogeneous field. It should be noted that the inhomogeneous field will change its direction on the negative semi-axis of the x axis due to the linear approximation. To avoid this unphysical phenomenon, we take the electric-field strength to be zero in the region of $x < -1/2\varepsilon$. Therefore, the potential is written as

$$V_{\text{laser}}(\vec{r}, t) = \int^{\vec{r}} d\vec{r} \cdot \vec{E}(\vec{r}, t)$$
$$= E_0 x(1 + \varepsilon x)f(t)\sin(\omega t + \phi). \tag{5}$$

To solve the 2D-TDSE numerically, we employ the spilt-operator spectral method on a Cartesian gird [60]. The initial wave function is obtained by imaginary-time propagation [61]. For the inhomogeneous field, when the wave function propagates to the end of the laser pulse, we split it into two parts: an inner region ($0 - R_c$) and outer region ($R_{\text{max}} - R_c$), where R_c is the absorbing boundary and R_{max} is the boundary of the whole grid space [62]. After the end of the laser pulse, we propagate the wave packet without field for two cycles. At the last time τ, $\Psi(\tau)$ is given by

$$\Psi(\tau) = \Psi(\tau)[1 - F_s(R_c)] + \Psi(\tau)F_s R_c$$
$$= \Psi(\tau)_{\text{in}} + \Psi(\tau)_{\text{out}}. \tag{6}$$

Here, $F_s(R_c) = 1/(1 + e^{-(r-R_c)/\Delta})$ is the absorbing function and δ is the width of the crossover region. $\Psi(\tau)_{\text{out}}$ represents the "ionized part." The wave-packet propagates for two cycles after the end of the laser pulse and is far from the nucleus. Thus the effect of the Coulomb potential can be neglected, and the wave packet $\Psi(\tau)_{\text{out}}$ can be transformed into momentum space as a plane wave,

$$C(\vec{p}, \tau) = \int \Psi(\tau)_{\text{out}} \frac{e^{-i\vec{p}\cdot\vec{r}}}{2\pi} d^2\vec{r}. \tag{7}$$
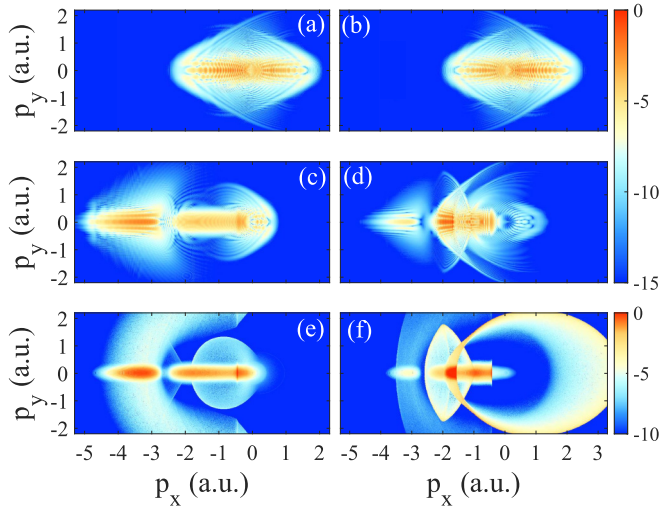
FIG. 1. (a), (b) The PEMDs (logarithmic scale) for strong-field tunneling ionization of a hydrogen atom ($I_p = 0.5$ a.u.) in an 1600-nm single-color laser field with intensity $I = 1 \times 10^{14}$ W/cm^2. The top row shows the results of the spatially homogeneous field ($\varepsilon = 0$) obtained by solving the TDSE. The middle and bottom rows correspond to the results of the spatially inhomogeneous field ($\varepsilon = 0.003$) obtained by (c), (d) the TDSE and (e), (f) the classical model, respectively. The left and right columns represent the results of (a), (c), (e) $\phi = 0$ and (b), (d), (f) $\phi = \pi$ of the laser field, respectively.

Then, the final PEMD is obtained by

$$\frac{dP(\vec{r})}{dE d\theta} = |C(\vec{p}, \tau)|^2, \tag{8}$$

where $E = |\vec{p}|^2/2$ is the final energy of electrons and θ is its emission angle.

In our simulation, the time step of propagation is $\Delta t = 0.2$ a.u. The Cartesian grid space ranges from -2000 a.u. to 2000 a.u. for both the x-axis and y-axis directions with a grid size of $\Delta x = \Delta y = 0.3$ a.u. The inner space boundary is $R_c = 200$ a.u. with $\Delta = 4$ a.u. The choice of R_c should be large enough so that the Coulomb potential is negligible. But if R_c is too large, some electron wave packets that propagate not far enough will be lost, and the low-energy part of the PEMD will be missing. Thus we choose $R_c = 200$ a.u., which is an appropriate size.

III. RESULTS AND DISCUSSIONS

In Fig. 1, we show the PEMDs for strong-field tunneling ionization of a hydrogen atom. Figure 1(a) shows the result in the 1600-nm homogeneous field with $I = 1 \times 10^{14}$ W/cm^2 and $\phi = 0$. Figure 1(c) displays the PEMD driven by an inhomogeneous field with the same laser parameters as Fig. 1(a). In Fig. 1(a), the momentum distribution is clustered in the region of $p_x \in [-3, 2]$ a.u. Due to the few-cycle pulse ($T_p = 4T$), the PEMD is asymmetric about $p_x = 0$ in homogeneous field. In Fig. 1(c), PEMD substantially shifts to the negative direction and reaches $p_x = -5$ a.u. Moreover, the energy of electrons with positive momentum is suppressed. This means that the electrons obtain extra kinetic energy by traveling in the inhomogeneous field, and the high-energy electrons only

focus on the region of negative momentum. In addition, the PEMD is distinctly separated at about $p_x = -2.6$ a.u. and these two parts represent electrons ionized in different half cycles (as will be explained below). Figures 1(b) and 1(d) are the same as Figs. 1(a) and 1(c), respectively, but for $\phi = \pi$. In the spatially homogeneous field, the PEMDs for $\phi = 0$ and $\phi = \pi$ are inversion symmetric, but this symmetry is broken in the inhomogeneous field [45].

Figures 1(e) and 1(f) show the results obtained from the classical model. In this simple model, the trajectory evolution is determined by solving the classical Newton equation of motion, and the influence of the Coulomb potential is neglected. At a given time, which called the ionization time t_i, the electron is released at the position $x(t_i) = 0$, $y(t_i) = 0$, with a zero longitudinal velocity $v_x(t_i) = 0$ and a nonzero transverse velocity v_y. The weight of the classical trajectories is given by the Ammosov-Delone-Krainov theory [63,64]. After being released, the electron is driven by the laser electric field and reaches the detector directly or through a rescattering process. For the latter, the electron returns back to the plane where the parent ion is located at the rescattering time t_r, i.e., $x(t_r) = 0$, and is elastically scattered at an angle which is assumed to be uniformly distributed between 0 and π. After the end of the laser field, the electron travels for two more cycles (about 440 a.u.) without the field. Finally, the classical trajectories of both the direct and rescattering electrons form the momentum distribution of the classical model. From Figs. 1(e) and 1(f), it is shown that the results from the simple classical model agree well with the TDSE results in Figs. 1(c) and 1(d).

With the classical model, the tunneling ionization time of electrons in different regions of the PEMD can be obtained. Thus we separately calculated the PEMD of electrons released from 1.5–2 T and 2–2.5 T by the classical model. The results are shown in Figs. 2(b) and 2(c), respectively. In Figs. 2(d) and 2(e), we show the enlarged views of the TDSE results in Fig. 1(c). It is shown that the electrons ionized in different half cycles are completely separated by the spatial inhomogeneity of the laser field. The electrons of the high-energy region are mostly ionized within 1.5–2 T, and the electrons ionized within 2–2.5 T are concentrated in the low-energy region. To show more intuitively the dynamic process of separation, we show the evolution of the classical electron momentum in Fig. 3. For the spatially homogeneous case in Fig. 3(a), the final momentum of the electrons ionized within 1.5–2 T (the thin light blue curves) and 2–2.5 T (the thick dark red curves) are distributed in the same region $p_x \in [-2, 1.5]$ a.u. But for the spatially inhomogeneous case in Fig. 3(b), the two parts are separated at about $p_x = -2.6$ a.u., which is consistent with the PEMDs from the TDSE and the classical model. It indicates that the separation is essentially due to the different initial motion directions. This phenomena is caused by the form of the spatial inhomogeneity of the electric field, namely $E(\vec{r}, t) = (1 + 2\varepsilon x)E(t)$. The strength of the electric field increases with the distance in the region of $x > 0$ but decreases as the distance increases in the region of $x < 0$. Thus, the electron moving in the positive direction can be affected by the stronger electric field and gain more energy from the field. But for the electron moving in the negative direction, it feels a much weaker field and thus achieves a
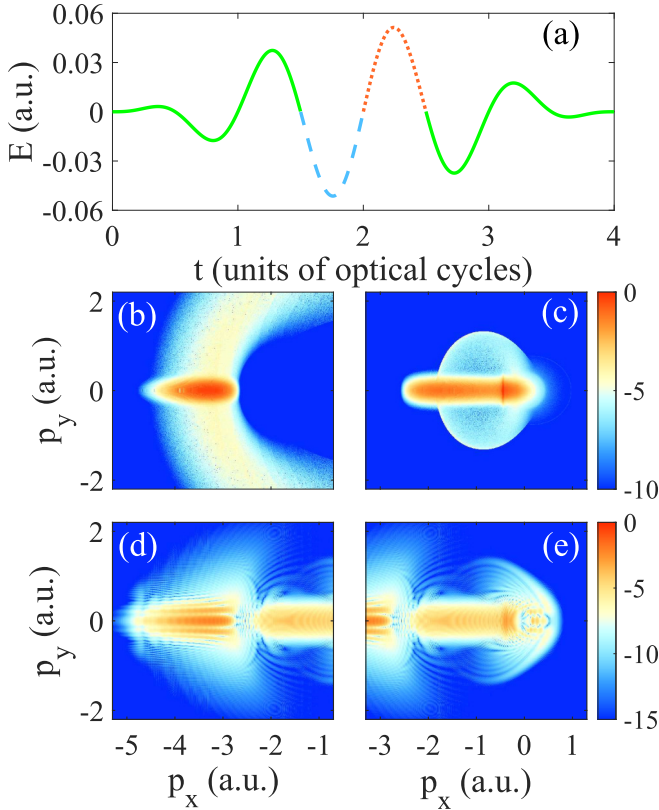
FIG. 2. (a) The electric field of the laser pulse at the origin. The middle and bottom rows are the PEMDs for strong-field tunneling ionization of a hydrogen atom. The middle row corresponds to the electron tunneled out within (b) 1.5–2 T [the dashed blue curve in panel (a)] and (c) 2–2.5 T [the dotted red curve in panel (a)], respectively, which is calculated by the classical model. (d), (e) The same as in panels (b) and (c) but calculated by the TDSE. The laser parameters are the same as in Fig. 1 and $\phi = 0$.

lower final energy. Therefore, the inhomogeneous field can provide an efficient tool to separate the electrons ionized in different cycles.

To analyze the interference structure, Fig. 4 shows the enlarged views of the interference patterns. Figures 4(a) and 4(c) enlarge the interference patterns on the left part of the PEMDs in Figs. 1(a) and 1(c), respectively. In Fig. 4(a), the
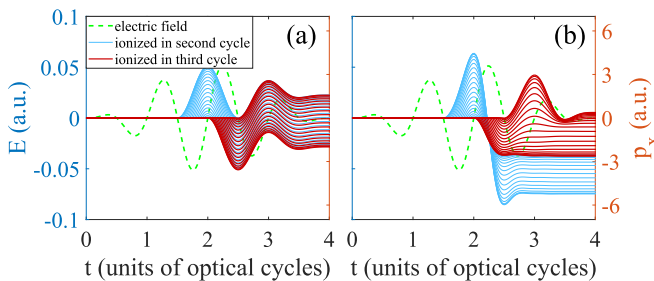

FIG. 3. The classical momentum evolution of the electrons tunneled out within 1.5–2 T (the thin light blue curves) and 2–2.5 T (the thick dark red curves), for the case of spatial (a) homogeneity and (b) inhomogeneity. The dashed green curves are the laser field at the origin. Its parameters are same as Fig. 1 and $\phi = 0$.
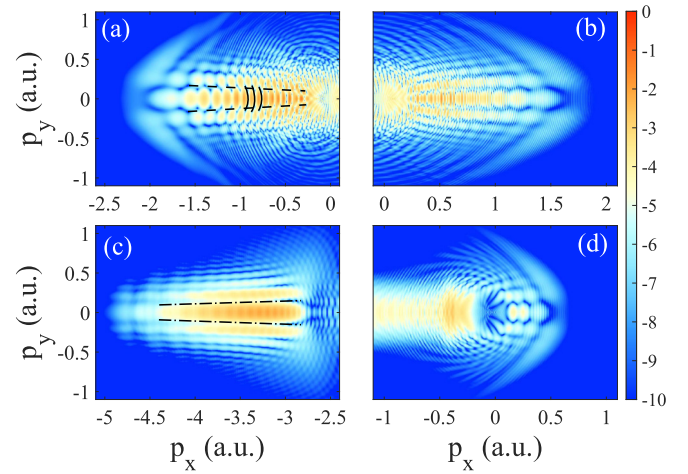

FIG. 4. (a), (b) Enlarged views of the interference patterns on the left and right parts of the PEMD in Fig. 1(a), respectively. (c), (d) Enlarged views of the interference patterns on the left and right in parts of the PEMD of Fig. 1(c), respectively.

nearly horizontal fringes (the dashed lines) are referred to the SFPH pattern, which originates from the interference of the direct electrons and the near-forward-scattering electrons. The other nearly vertical fringes (the solid curves) come from the interference of the direct electrons tunneling ionized during two adjacent quarter cycles of the laser pulse [65,66] and are identified as the intracycle interference. However, for the spatially inhomogeneous case, as shown in Fig. 4(c), the intracycle interference pattern becomes invisible. In other words, the electrons in the high-energy region come from a single half cycle, and these electrons do not interfere with other electrons ionized in adjacent quarter cycles. Moreover, the holographic fringes in Fig. 4(c) (the dot-dashed lines) shrink as p_x increases, which is the opposite of that in the homogeneous field. This is because the relationship between the travel time and the final momentum is different in the two cases, as will be analyzed below. The interferences of the electrons ionized within 2–2.5 T are shown in Figs. 4(b) (the homogeneous field) and 4(d) (the inhomogeneous field). It is shown that, for the homogeneous field, the holographic interference still exists, while it is strongly suppressed for the inhomogeneous field. The intracycle interference can only be observed at low electron energies in the inhomogeneous field [39].

The holographic pattern is determined by the phase difference between the direct and the near-forward rescattering electrons, which can be written as [21,22,28–30]

$$\Delta\varphi(p_y) = \tfrac{1}{2} p_y^2 (t_r - t_i) + \alpha + O(\zeta^1). \qquad (9)$$

The first term corresponds to the phase difference between the direct and rescattering electrons accumulated during the propagation in the laser field, where t_i and t_r are the ionization and rescattering time, respectively. The ionization time is determined by the time of the electron released from the atom, and the rescattering time is obtained when the electron returns back to the plane that contains the parent ion and is perpendicular to the direction of the electron motion. The first term has been revealed by the strong-field approximation
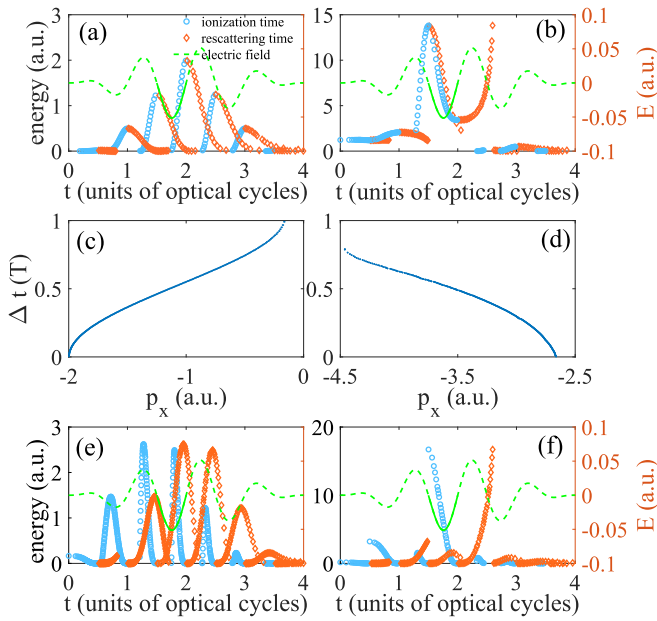
FIG. 5. Classical electron final kinetic energies as a function of the ionization (blue dots) and rescattering (red diamonds) times in the (a) homogeneous and (b) inhomogeneous fields, respectively. The shaded parts represent the ionization time window of the rescattering electrons which can be retrieved. The middle row shows the travel time between ionization and scattering as a function of the final momentum for the spatial (c) homogeneity and (d) inhomogeneity, respectively. (e), (f) The same as panels (a) and (b), respectively, but for the rescattering energies. The dashed green curves are the laser field at the origin. The laser parameters are same as in Fig. 1 and $\phi = 0$.

and the semiclassical trajectory model [10,18,20]. It makes the largest contribution to the phase difference. Furthermore, the difference of the holographic fringes between the homogeneous and inhomogeneous fields is mainly caused by this term, namely, the travel time $(t_r - t_i)$. The second term α is the phase of the scattering amplitude, which denotes the phase of the rescattering electrons obtained during scattering with the parent ion [21]. The third term $\zeta \sim \omega / I_p$ is a small term that can be ignored [21].

To analyze the dynamics of electrons in the PEMDs, we trace the classical trajectories of the near-forward rescattering electrons. Figures 5(a) and 5(b) show the final energy of electron as a function of the tunneling ionization time (blue dots) and the rescattering time (red diamonds), in the homogeneous and inhomogeneous fields, respectively. In Fig. 5(a), only electrons ionized along the falling edge of the electric field can be scattered, and the maximum kinetic energy is about 2 a.u. But in the inhomogeneous field, it is shown that all electrons ionized during 1.5–2 T can be scattered, and the kinetic energy can reach 13.7 a.u., which is much higher than that in the homogeneous field. For electrons ionization during other laser cycles, the final energy is much lower. Thus, the holographic interference in Fig. 4(c) is exclusively from the electrons ionized during 1.5–2 T. Furthermore, it has been shown that the SFPH could be employed to probe the attosecond electron dynamics in atoms and molecules [22]. There, the electron dynamics during the time window for tunneling

ionization of the rescattering electrons could be retrieved. In the homogeneous field, the time window is about 1/8 of a cycle, as shown in Fig. 5(a). However, for the inhomogeneous field, the time window is as wide as 1/4 cycle, as shown in Fig. 5(b). It means that the inhomogeneous field provides a broaden time window for probing the electron dynamic with SFPH.

In Figs. 5(c) and 5(d), we show the travel time between ionization and rescattering of the electrons liberated within 1.5–2 T (green solid curve) in homogeneous and inhomogeneous fields, respectively. From Eq. (9), it can be seen that the phase difference of the holographic fringes depends on the travel time. For the case of the spatial homogeneity, the fork-like structure of the holographic interference in Fig. 4(a) is caused by the travel time decreases as the final momentum increases. However, in the inhomogeneous field, the travel time increases with p_x, which causes the interference fringes to shrink as p_x increase in Fig. 4(c), as opposed to that in the homogeneous field. Therefore, the difference in time changes with p_x in the two cases leads to the difference in the holographic fringes.

In probing the atomic and molecular structure and electron dynamics with rescattering electrons, the returning kinetic energy is a very important parameter. In Figs. 5(e) and 5(f), we show the returning energy of electron as a function of the tunneling ionization time (blue dots) and the rescattering time (red diamonds), in the homogeneous and inhomogeneous fields, respectively. For the energy as a function of the ionization time in Fig. 5(e), the left and right arms of peaks have positive and negative slopes with different ionization times, which are the long and short paths, respectively. In the inhomogeneous field, the long path disappears, and the returning energy is mainly contributed by the short path [42,45]. It indicates that the electron ionized at earlier times and scattered at later times can gain more rescattering energy. The returning energy of the electrons ionized during 1.5–2 T can be up to 16.4 a.u. ($18.7 U_p$), much higher than 2.67 a.u. ($3.05 U_p$) in the homogeneous field. As shown in Fig. 6, the electron ionized during 1.5–2 T moves in the positive direction [dashed red curve in Fig. 6(a)]. Due to the linear form of the spatial inhomogeneity, as the distance from the origin increases, the electron is subjected to a stronger the electric field [dotted blue curve in Fig. 6(b)]. It should be noted that the largest distance the electrons can reach is about 400 a.u., where the maximum field enhancement factor is about 3.5. After the electric field reverses its direction, the electron is adequately accelerated by the electric field with a strong intensity and returns back to the parent ion with a large energy [dot-dashed violet curve in Fig. 6(c)]. When this electron moves into the negative semi-axis, the strength of the electric field becomes too small to reduce the high kinetic energy of this electron. This explains why the electron can obtain much higher rescattering energy and final energy than that in the homogeneous field. Moreover, the high returning energy can also influence the scattering process. For example, it can reduce the scattering angle of the electrons at the same location. Consequently, the density of the PEMD near $p_y = 0$ for the inhomogeneous field is higher than that in the homogeneous field.
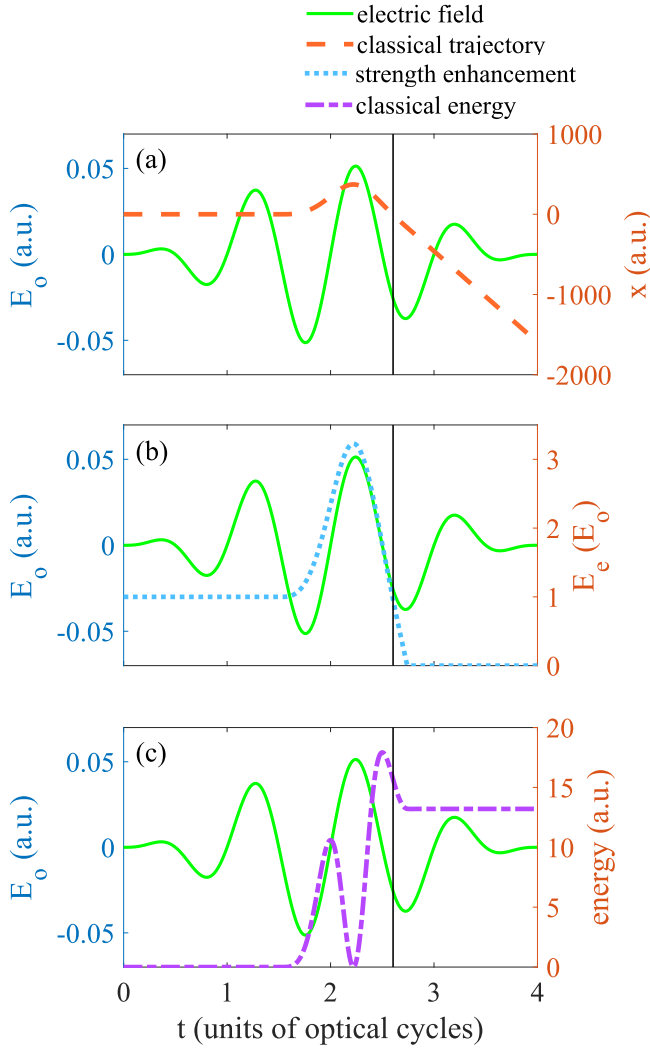
FIG. 6. The evolution of (a) the classical trajectory and (c) the classical energy of the electron which has the high rescattering energy and final energy, and this electron is released at about 1.6 T. (b) The strength enhancement evolution of the electric field the electron feels, where E_o is the electric field at the origin. The vertical solid black lines indicate the time when the electron return back to the parent ion. The solid green curves are the laser field at the origin. The laser parameters are the same as in Fig. 1.

Finally, we study the effect of ε and the CEP on PEMDs. Figure 7 shows the PEMDs for different ε. As expected, the stronger the spatial inhomogeneity, the higher the final kinetic momentum. On the other hand, with the increase of the spatial inhomogeneity, the electrons ionized in different cycles are gradually separated. In the case of $\varepsilon = 0.003$, the distinct dividing line appears, and the holographic fringes change significantly. Figure 8 shows the PEMDs for the different CEPs. It can be seen that the PEMDs are very sensitive to the CEP [38]. As the CEP changes from 0 to π, the interference structure becomes more complex, and the separated part on the left in the PEMD gradually disappears. For $\phi = 0.8\pi - \pi$, the electrons ionized during 1.5–2.5 T are concentrated in the region of $p_x \in [-2, -0.5]$ a.u., and the separated part on the left is formed by the electrons ionized within 1–1.5 T,
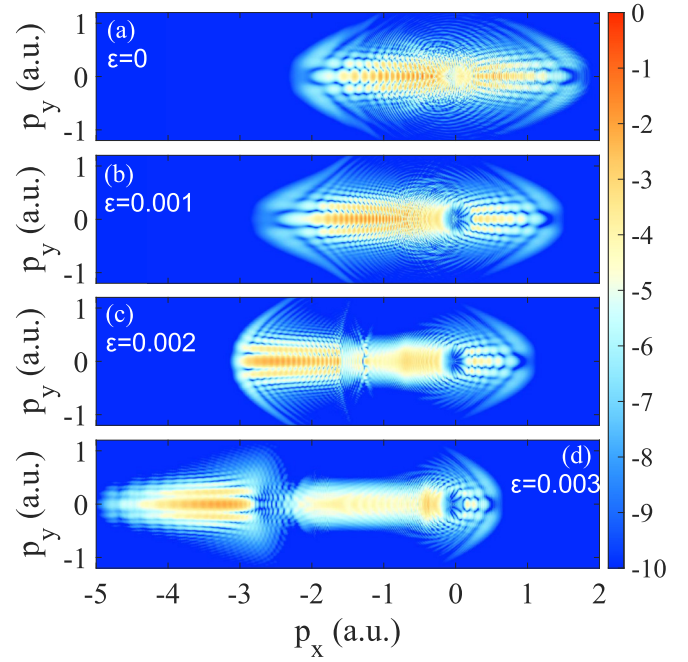

FIG. 7. The PEMDs for strong-field tunneling ionization of a hydrogen atom for (a) $\varepsilon = 0$ (homogeneous field), (b) $\varepsilon = 0.001$, (c) $\varepsilon = 0.002$, and (d) $\varepsilon = 0.003$. The laser parameters are the same as in Fig. 1.

where the ionization probability is low. The former leads to the complexity of the interference structures, and the latter results in the reduction of the density of the separated part on the left. Then as the CEP goes from π to 2π, the parts of the electrons coming from the different cycles are separated again. In general, by changing ε and the CEP, the effect of the spatial inhomogeneity on the electron trajectory can be controlled. Completely separating electrons ionized in different cycles requires the laser field with a strong enough spatial inhomogeneity and an appropriate CEP.

In our calculations, the inhomogeneous field was approximated as a linear form. Our extra calculations show that, in the more realistic inhomogeneous fields, such as those in the vicinity of the nanotip illuminated by a laser pulse, the main properties of the PEMDs, i.e., the separation of the holograms, the enhancement of the electron energy, and the change of the holographic fringes, are similar to the results for the linear approximation.

IV. CONCLUSIONS

In this paper we study the strong-field photoelectron holography in the inhomogeneous field. The spatially inhomogeneous field can be generated, for example, in the vicinity of the metal nanotip irradiated by a laser field. In our model, we use the linear approximation for the inhomogeneous field to demonstrate the control of the spatial inhomogeneity on the strong-field photoelectron holography. The photoelectron momentum distribution for a hydrogen atom is obtained by numerically solving the 2D-time-dependent Schrödinger equation. It is shown that the final kinetic energy of the electron is substantially increased. With the classical model,
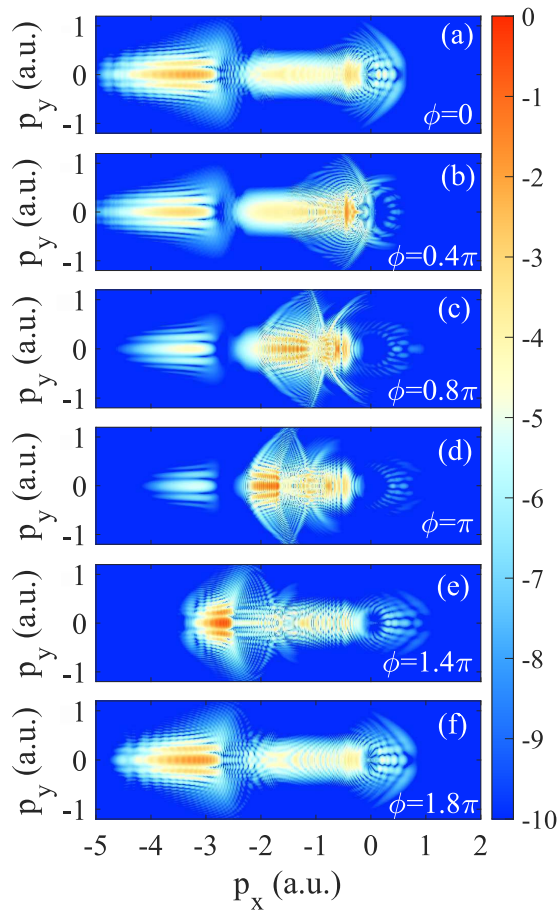
FIG. 8. The PEMDs for strong-field tunneling ionization of a hydrogen atom in the inhomogeneous field ($\varepsilon = 0.003$). The laser parameters are same as Fig. 1 but for (a) $\phi = 0$, (b) 0.4π, (c) 0.8π, (d) π, (e) 1.4π, and (f) 1.8π.

we find that the electrons released in different cycles gain different energies and are separated in momentum space. In addition, we show that the electrons in the inhomogeneous field could achieve much higher returning energy and final energy than those in the homogeneous field. Through the analysis of the relationship between ionization time and final energy, it is shown that the time window of tunneling ionization wherein the electrons could be driven back to induce holography is broaden in the inhomogeneous field. By changing the spatially inhomogeneous strength and the carrier envelope phase, we demonstrate that the electron trajectories can be controlled. The details of these phenomena depend on the form of the spatially inhomogeneous field. Therefore, it will have different details if the electron driven by the field with other forms of the spatial inhomogeneity. But the main properties of the holography in the inhomogeneous fields, i.e., the separation of the holograms from different half laser cycles, the enhancement of the electron energy and the change of the holographic fringes, will be reserved for different forms of the spatial inhomogeneity. Our results show the effect of the inhomogeneous field on the electron trajectory. These interesting properties will benefit the application of strong-field photoelectron holography.

[1] A. McPherson, G. Gibson, H. Jara, U. Johann, T. S. Luk, I. A. McIntyre, K. Boyer, and C. K. Rhodes, J. Opt. Soc. Am. B **4**, 595 (1987).

[2] W. Becker, F. Grasbon, R. Kopold, D. B. Milošević, G. G. Paulus, and H. Walther, Adv. At. Mol. Phys. **48**, 35 (2002).

[3] B. Walker, B. Sheehy, L. F. DiMauro, P. Agostini, K. J. Schafer, and K. C. Kulander, Phys. Rev. Lett. **73**, 1227 (1994).

[4] Y. Zhou, Q. Liao, and P. Lu, Phys. Rev. A **82**, 053402 (2010).

[5] P. B. Corkum, Phys. Rev. Lett. **71**, 1994 (1993).

[6] F. Krausz and M. Ivanov, Rev. Mod. Phys. **81**, 163 (2009).

[7] G. Sansone, E. Benedetti, F. Calegari, C. Vozzi, L. Avaldi, R. Flammini, L. Poletto, P. Villoresi, C. Altucci, R. Velotta *et al.*, Science **314**, 443 (2006).

[8] T. Morishita, A.-T. Le, Z. Chen, and C. D. Lin, Phys. Rev. Lett. **100**, 013903 (2008).

[9] J. Itatani, J. Levesque, D. Zeidler, Hiromichi Niikura, H. Pépin, J. C. Kieffer, P. B. Corkum, and D. M. Villeneuve, Nature (London) **432**, 867 (2004).

[10] Y. Huismans, A. Rouzée, A. Gijsbertsen, J. H. Jungmann, A. S. Smolkowska, P. S. W. M. Logman, F. Lépine, C. Cauchy, S. Zamith, T. Marchenko *et al.*, Science **331**, 61 (2011).

[11] D. D. Hickstein, P. Ranitovic, S. Witte, X. M. Tong, Y. Huismans, P. Arpin, X. Zhou, K. E. Keister, C. W. Hogle, B. Zhang *et al.*, Phys. Rev. Lett. **109**, 073004 (2012).

[12] D. G. Arbó, C. Lemell, S. Nagele, N. Camus, L. Fechner, A. Krupp, T. Pfeifer, S. D. López, R. Moshammer, and J. Burgdörfer, Phys. Rev. A **92**, 023402 (2015).

[13] L. Fechner, N. Camus, A. Krupp, J. Ullrich, T. Pfeifer, and R. Moshammer, Phys. Rev. A **92**, 051403(R) (2015).

[14] H. Xie, M. Li, S. Luo, Y. Li, J. Tan, Y. Zhou, W. Cao, and P. Lu, Opt. Lett. **43**, 3220 (2018).

[15] M. Meckel, A. Staudte, S. Patchkovskii, D. M. Villeneuve, P. B. Corkum, R. Dörner, and M. Spanner, Nat. Phys. **10**, 594 (2014).

[16] J. Tan, S. Xu, X. Han, Y. Zhou, M. Li, W. Cao, Q. Zhang, and P. Lu, Adv. Photon. **3**, 035001 (2021).

[17] J. Tan, Y. Zhou, M. He, Q. Ke, J. Liang, Y. Li, M. Li, and P. Lu, Phys. Rev. A **99**, 033402 (2019).

[18] M.-M. Liu, M. Li, C. Wu, Q. Gong, A. Staudte, and Y. Liu, Phys. Rev. Lett. **116**, 163004 (2016).

[19] M. Li, H. Xie, W. Cao, S. Luo, J. Tan, Y. Feng, B. Du, W. Zhang, Y. Li, Q. Zhang *et al.*, Phys. Rev. Lett. **122**, 183202 (2019).

[20] Y. Huismans, A. Gijsbertsen, A. S. Smolkowska, J. H. Jungmann, A. Rouzée, P. S. W. M. Logman, F. Lépine,

C. Cauchy, S. Zamith, T. Marchenko *et al.*, Phys. Rev. Lett. **109**, 013002 (2012).

[21] Y. Zhou, O. I. Tolstikhin, and T. Morishita, Phys. Rev. Lett. **116**, 173001 (2016).

[22] M. He, Y. Li, Y. Zhou, M. Li, W. Cao, and P. Lu, Phys. Rev. Lett. **120**, 133204 (2018).

[23] M. He, Y. Li, Y. Zhou, M. Li, and P. Lu, Phys. Rev. A **93**, 033406 (2016).

[24] C. Faria and A. S. Maxwell, Rep. Prog. Phys. **83**, 034401 (2020).

[25] X.-B. Bian and A. D. Bandrauk, Phys. Rev. Lett. **108**, 263003 (2012).

[26] Q. Ke, Y. Zhou, J. Tan, M. He, J. Liang, Y. Zhao, M. Li, and P. Lu, Opt. Express **27**, 32193 (2019).

[27] Y. Zhou, J. Tan, M. Li, and P. Lu, Sci. China: Phys., Mech. Astron. **64**, 273011 (2021).

[28] S. D. López and D. G. Arbó, Phys. Rev. A **100**, 023419 (2019).

[29] N. Werby, A. S. Maxwell, R. Forbes, P. H. Bucksbaum, and C. Figueira de Morisson Faria, Phys. Rev. A **104**, 013109 (2021).

[30] G. Porat, G. Alon, S. Rozen, O. Pedatzur, M. Krüger, D. Azoury, A. Natan, G. Orenstein, B. D. Bruner, M. J. J. Vrakking, and N. Dudovich, Nat. Commun. **9**, 2805 (2018).

[31] G. Herink, D. R. Solli, M. Gulde, and C. Ropers, Nature (London) **483**, 190 (2012).

[32] M. F. Ciappina, J. A. Pérez-Hernández, A. S. Landsman, W. A. Okell, S. Zherebtsov, B. Förg, J. Schötz, L. Seiffert, T. Fennel, T. Shaaran *et al.*, Rep. Prog. Phys. **80**, 054401 (2017).

[33] I. N. Ansari, M. S. Mrudul, M. F. Ciappina, M. Lewenstein, and G. Dixit, Phys. Rev. A **98**, 063406 (2018).

[34] M. F. Ciappina, J. A. Pérez-Hernández, T. Shaaran, J. Biegert, R. Quidant, and M. Lewenstein, Phys. Rev. A **86**, 023413 (2012).

[35] Z. Wang, P. Lan, J. Luo, L. He, Q. Zhang, and P. Lu, Phys. Rev. A **88**, 063838 (2013).

[36] A. Chacón, M. F. Ciappina, and M. Lewenstein, Phys. Rev. A **94**, 043407 (2016).

[37] T. Shaaran, M. F. Ciappina, and M. Lewenstein, Phys. Rev. A **87**, 053415 (2013).

[38] M. F. Ciappina, J. A. Pérez-Hernández, T. Shaaran, L. Roso, and M. Lewenstein, Phys. Rev. A **87**, 063833 (2013).

[39] L. Ortmann, J. A. Pérez-Hernández, M. F. Ciappina, J. Schötz, A. Chacón, G. Zeraouli, M. F. Kling, L. Roso, M. Lewenstein, and A. S. Landsman, Phys. Rev. Lett. **119**, 053204 (2017).

[40] I. N. Ansari, C. Hofmann, L. Medišauskas, M. Lewenstein, M. F. Ciappina, and G. Dixit, Phys. Rev. A **103**, 013104 (2021).

[41] A. Husakou, S.-J. Im, and J. Herrmann, Phys. Rev. A **83**, 043839 (2011).

[42] M. F. Ciappina, J. Biegert, R. Quidant, and M. Lewenstein, Phys. Rev. A **85**, 033828 (2012).

[43] S. Kim, J. Jin, Y.-J. Kim, I.-Y. Park, Y. Kim, and S.-W. Kim, Nature (London) **453**, 757 (2008).

[44] M. F. Ciappina, S. S. Aćimović, T. Shaaran, J. Biegert, R. Quidant, and M. Lewenstein, Opt. Express **20**, 26261 (2012).

[45] I. Yavuz, E. A. Bleda, Z. Altun, and T. Topcu, Phys. Rev. A **85**, 013416 (2012).

[46] A. Farmani, S. Sarikhani, and S. Batebi, Opt. Commun. **439**, 47 (2019).

[47] H. Zhong, J. Guo, W. Feng, P.-C. Li, and X.-S. Liu, Phys. Lett. A **380**, 188 (2016).

[48] L.-J. Lü and X.-B. Bian, Phys. Rev. A **102**, 033110 (2020).

[49] T.-Y. Du, Z. Guan, X.-X. Zhou, and X.-B. Bian, Phys. Rev. A **94**, 023419 (2016).

[50] T. Shaaran, M. F. Ciappina, and M. Lewenstein, Phys. Rev. A **86**, 023408 (2012).

[51] L. Seiffert, T. Paschen, P. Hommelhoff, and T. Fennel, J. Phys. B: At., Mol. Opt. Phys. **51**, 134001 (2018).

[52] E. Neyra, F. Videla, M. F. Ciappina, J. A. Pérez-Hernández, L. Roso, M. Lewenstein, and G. A. Torchia, J. Opt. (Bristol, U.K.) **20**, 034002 (2018).

[53] M. F. Ciappina, T. Shaaran, R. Guichard, J. A. Pérez-Hernández, L. Roso, M. Arnold, T. Siegel, A. Zaïr, and M. Lewenstein, Laser Phys. Lett. **10**, 105302 (2013).

[54] L. Ortmann and A. S. Landsman, Phys. Rev. A **97**, 023420 (2018).

[55] M. Yamaguchi and K. Nobusada, Phys. Rev. A **93**, 023416 (2016).

[56] I. Yavuz, M. F. Ciappina, A. Chacón, Z. Altun, M. F. Kling, and M. Lewenstein, Phys. Rev. A **93**, 033404 (2016).

[57] P. Rueda, F. Videla, E. Neyra, J. A. Pérez-Hernández, M. F. Ciappina, and G. A. Torchia, J. Phys. B: At., Mol. Opt. Phys. **53**, 065403 (2020).

[58] C. Zhang, C. Liu, and Z. Xu, Phys. Rev. A **88**, 035805 (2013).

[59] M. F. Ciappina, J. A. Pérez-Hernández, L. Roso, A. Zaïr, and M. Lewenstein, J. Phys.: Conf. Ser. **601**, 012001 (2015).

[60] M. D. Feit, J. A. Fleck, and A. Steiger, J. Comput. Phys. **47**, 412 (1982).

[61] M. Protopapas, C. H. Keitel, and P. L. Knight, Rep. Prog. Phys. **60**, 389 (1997).

[62] S. Chelkowski, C. Foisy, and A. D. Bandrauk, Phys. Rev. A **57**, 1176 (1998).

[63] M. V. Ammosov, N. B. Delone, and V. P. Krainov, Sov. Phys. JETP **64**, 1191 (1986).

[64] N. B. Delone and V. P. Krainov, J. Opt. Soc. Am. B **8**, 1207 (1991).

[65] D. G. Arbó, E. Persson, and J. Burgdörfer, Phys. Rev. A **74**, 063407 (2006).

[66] M. Richter, M. Kunitski, M. Schöffler, T. Jahnke, L. P. H. Schmidt, M. Li, Y. Liu, and R. Dörner, Phys. Rev. Lett. **114**, 143001 (2015).